applied sciences

MDPI

Article

High Density RF-DC Plasma Nitriding under Optimized Conditions by Plasma-Diagnosis

Tatsuhiko Aizawa [1,*], Imron Rsadi [2] and Ersyzario Edo Yunata [3]

[1] Surface Engineering Design Laboratory, SIT, Tokyo 144-0045, Japan
[2] University of Brawijaya, Malang 65145, Indonesia; almiron@student.ub.ac.id
[3] Airlangga University, Surabaya 60115, Indonesia; ersyzario.edo@fst.unair.ac.id
* Correspondence: taizawa@sic.shibaura-it.ac.jp; Tel.: +81-3-6424-8615

Featured Application: Efficient plasma nitriding of stainless steels at low temperature under optimized processing conditions by plasma-diagnosis.

Abstract: This paper is concerned with plasma diagnosis on a N_2-H_2 gas mixture to determine the optimum parameters for the nitriding process. Plasma parameters such as pressure, RF-voltage, and DC-bias were varied for optimization. The active species such as N_2^+ and NH were identified in plasma diagnosis. In the N_2-H_2 gas mixture, hydrogen imposed a great influence on plasma generation. The small addition of a hydrogen molecule into the gas mixture resulted in the highest yield of N_2^+ ions and NH radicals; the optimum hydrogen content was 20% in the mixture. The austenitic stainless-steel type AISI304 was nitrided at 673 K and 623 K to experimentally demonstrate that hydrogen gas content optimization is necessary to improve the surface hardness and to describe low temperature nitriding under high nitrogen flux at the surface.

Keywords: plasma diagnosis; nitrogen-hydrogen gas mixture; hydrogen gas content; AISI304 stainless steels; surface hardness; nitrogen supersaturation; inner nitriding behavior

Citation: Aizawa, T.; Rsadi, I.; Yunata, E.E. High Density RF-DC Plasma Nitriding under Optimized Conditions by Plasma-Diagnosis. *Appl. Sci.* **2022**, *12*, 3706. https://doi.org/10.3390/app12083706

Academic Editor: Emilio Martines

Received: 1 November 2021
Accepted: 6 April 2022
Published: 7 April 2022

1. Introduction

Low temperature plasma nitriding has been widely studied and applied to stainless steels since it was first reported in [1]. As summarized in [2–4], various results have been reported in the literature on the plasma nitriding of AISI420 type stainless steels (SS) [5,6], AISI304 type SS [7,8] and AISI316 type SS [9,10]. This nitriding process forms the nitrogen supersaturated thick layer without nitride precipitates related to these stainless steels. After [4], the nitrogen supersaturated layer, with an average nitrogen content of 4.5 mass %, was formed to have a thickness of 50 μm by nitriding at 673 K for 14.4 ks. The yield of this thick nitrided layer with high nitrogen solute content was strongly dependent on the plasma processing conditions. However, a few papers have been concerned with the nitrogen–hydrogen plasma diagnosis to describe the nitrogen supersaturation process in low temperature plasma nitriding [4,11,12].

There are many plasma diagnosis tools to characterize the plasma nitriding state; e.g., electrostatic probe, optical emission spectroscopy (OES), laser-induced fluorescence (LIF), and absorption spectroscopy after [13]. Among them, OES is suitable for the diagnosis to measure the population of a species and describe various reaction processes in the plasma nitriding or surface activation process [14]. The active species such as N_2, N_2^+, NH radical and H were detected to investigate the plasma state in nitriding [15]. In particular, those species are more activated when using a hollow cathode device, as reported in [16,17]. On the other hand, the ion and radical nitriding processes utilized the N_2 + H_2 gas flow rate ratio by one to three in a similar manner to use the ammonia gas (NH_3) as a nitrogen and hydrogen resource [18].

In the present study, the RF (Radiofrequency)-DC (Direct Current) plasma nitriding system is utilized to investigate the effect of the hydrogen-to-nitrogen molar ratio to the activated species in plasmas. First, OES is employed to perform a plasma diagnosis on the effect of plasma processing parameters onto plasma activation, with and without the use of the hollow cathode device. Secondly, the hydrogen-to-nitrogen molar ratio is controlled to describe the variation in NH-radical intensity in OES. The AISI304 stainless steel specimen is nitrided at 673 K for 14.4 ks to demonstrate that the highest surface hardness is obtained under the optimum hydrogen-to-nitrogen molar ratio. Finally, the AISI304 specimen is nitrided at 623 K for 14.4 ks with the use of a hollow cathode to prove that this optimization is necessary to perform effective nitriding of stainless steels at lower holding temperatures.

2. Experimental Procedure

A RF-DC plasma nitriding system (YS-Electrics, Co., Ltd.; Yamanashi, Japan) is used and its processing functions are described. The plasma nitriding procedure is explained in detail. OES (Hamamatsu Photonics, Co., Ltd.; Shizuoka, Japan) is instrumented to measure the emissive light spectra from the plasmas. Materials characterization is also used to analyze the nitrided AISI304 specimen.

2.1. RF-DC Plasma Nitriding System

Figure 1 illustrates the plasma nitriding system with instrumentation of OES. This system consists of a stainless-steel chamber with a diameter of 500 mm and a height of 500 mm, mass flow control (MFC), dipole electrodes for ignition of RF-plasmas, a vacuum pump and a DC bias plate. Unlike conventional DC- or RF- plasma generators, there is no mechanical matching box. The input and output powers are automatically matched by frequency self-adjustment around 2 MHz. The plasma discharging is ignited by the dipole electrodes for RF-generation and by the DC bias for DC-application.

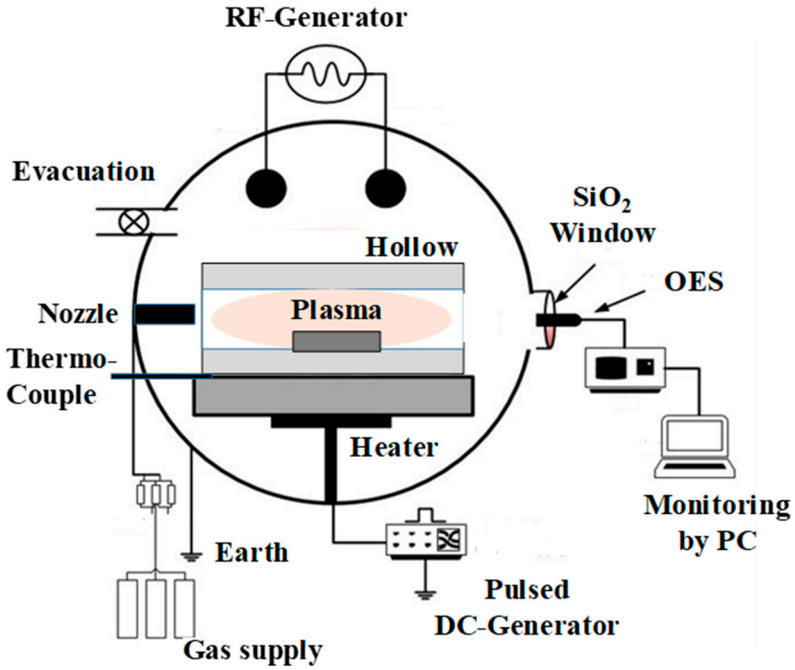

Figure 1. RF-DC plasma nitriding system with instrumentation of OES for monitoring the emissive light spectra from N_2 + H_2 plasmas.

In the nitriding experiments, the chamber was evacuated down to the base pressure of 0.1 Pa and the gas mixture was introduced inside the chamber. The flow ratio was adjusted by MFC. The hydrogen gas flow rate ratio in the mixture varied from 5% to 50%. The pressure (P) varied from 30 to 80 Pa. The RF-voltage (V_{RF}) varied from 100 to 250 V. The DC bias (V_{DC}) varied from −300 to −500 V. The nitrogen and hydrogen gases were mixed

for generating the plasma for nitriding. In the screening studies before this experiment, the plasma parameter was selected to be 35 Pa for pressure, −600 V for DC-bias, and 250 V for RF-voltage, respectively. In the nitriding experiments of AISI304 stainless steels, the holding temperature varied between 673 K and 623 K and the duration time was constant by 14.4 ks. The optimized hydrogen flow rate was employed in both nitriding experiments.

2.2. Plasma Diagnosis by OES

The active species in plasma was analyzed by OES. The optical detector was mounted onto a silica glass window in the plasma nitriding system. The signal was captured by an optical sensor and transferred to the personal computer. Two types of measurements were performed for wide scanning from 190 nm to 850 nm by the resolution of 1 nm, and for narrow scanning from 320 to 340 nm with the resolution of 0.1 nm. The spectrum was analyzed with the use of an NIST data base and reference data to identify each peak in the measured spectrum. Among those references, the experimental data by [14] was utilized. Table 1 lists the typical analyzed spectrum data for N_2 + H_2 plasmas. After rational deconvolution of the measured spectra, each species is identified at the specified position with significant intensity.

Table 1. Reference data for generated species by N_2 + H_2 plasmas.

Species	Transition Array	Peak Position (nm)
N_2^*	$B^3\prod_g \rightarrow A^3\sum_U$	580.4 ($v' = 11$, $v'' = 7$)
		775.3 ($v' = 2$, $v'' = 0$)
N_2^*	$C^3\prod_u$–$B^3\prod_g$	337.1 ($v' = 0$, $v'' = 0$)
		380.5 ($v' = 0$, $v'' = 2$)
N_2^+	$B^2\Sigma_u^+ - X^2\Sigma_g^+$	391.4 ($v' = 0$, $v'' = 0$)
		427.8 ($v' = 0$, $v'' = 1$)
H	Balmer series	656.3 (H_α)
		486.1 (H_β)
NH	Λ-sys $a^3\prod$-$X^3\sum^-$	336.01 ($v' = 0$, $v'' = 0$)

Where N_2* denotes for the activated nitrogen molecule.

2.3. Materials Characterization

In the nitriding experiments, SEM (Scanning Electron Microscopy; JSM-6060KU; JEOL Co., Ltd., Tokyo, Japan) with EDX (Electron Dispersive X-ray spectroscopy) was utilized to describe the cross-sectional microscopy and nitrogen mapping of nitrided AISI304 stainless steel specimens. EBSD (Electron Back-Scattering Diagram; JOEL, Tokyo, Japan) was also employed to analyze the inverse pole figure (IPF), the kernel angle misorientation (KAM) and the phase mapping of the nitrided layer. The hardness was measured by the micro-Vickers hardness tester (Mitsutoyo, Kawasaki, Japan).

3. Experimental Results and Discussion

N_2 + H_2 plasma diagnosis was performed by controlling the plasma processing parameters (RF-voltage, DC-bias and N_2 + H_2 gas pressure) to describe their effects on the mother nitrogen molecule ion or N_2^+. OES measurement was adjusted to accurately measure the NH-radicals by diagnosis. The hydrogen content was controlled to describe the effect of hydrogen-to-nitrogen molar ratio on the intensity of NH-radicals. AISI304 stainless steel substrates were plasma nitrided, respectively, at 673 K and 623 K for 14.4 ks to demonstrate that optimization of the hydrogen-to-nitrogen molar ratio was needed to ensure nitrogen supersaturation with sufficient nitrogen content and to harden the stainless steels, even at a low holding temperature.

3.1. Plasma Diagnosis on N_2 + H_2 Plasmas by OES

The plasma diagnosis under the various RF-voltages, DC-biases, and pressures was made with and without the hollow cathode setup. The measured spectrum of N_2-H_2 plasmas is shown in Figure 2. This spectrum was analyzed with the use of the reference in Table 1.

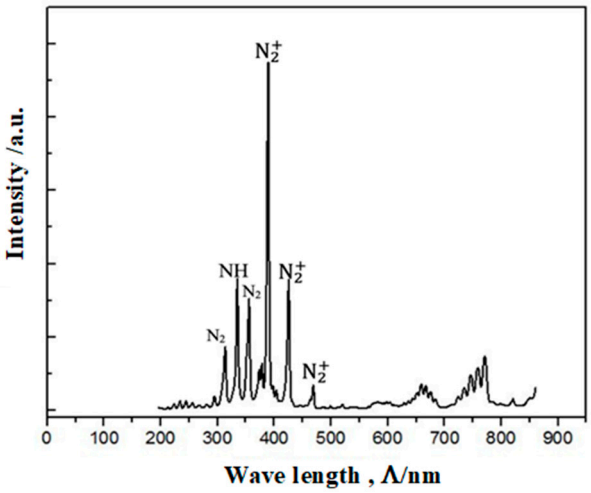

Figure 2. A typical spectrum of N_2 + H_2 plasmas by OES.

The highest intensity peak was detected at Λ = 391.4 nm for N_2^+ ions. The other species ware also detected at Λ = 580.4 nm for neutral N_2 molecule, and at Λ = 336.0 nm for NH radicals, respectively. This identification of NH-radicals is discussed later. In the above spectrum, N_2^+ is a mother species used to generate other nitrogen ions. This mother ion is yielded by the ionization reaction sequence by collisions between electrons and N_2 molecules. Following the study in [14], when a single electron collides with N_2 molecules, the kinetic energy of the electron ionizes the molecule at the specified energy level by releasing two electrons. The reaction can be written as follows:

$$e + N_2(A^3 \sum_u^+) \rightarrow N_2^+ + e + e \quad (1)$$

$$e + N_2(a' \sum_u^-) \rightarrow N_2^+ + e + e \quad (2)$$

$$e + N_2\left(B^3\Pi_g\right) \rightarrow N_2^+ + e + e \quad (3)$$

In this cascading reaction between electrons and neutral nitrogen molecules, the N_2^+ yield becomes the highest among various species in the N_2 + H_2 plasmas.

3.2. Effect of Plasma-Processing Parameters on the Active Species

RF-voltage, DC-bias and pressure work as the main plasma processing parameters to determine the population of generated species. In addition, when using the hollow cathode setup, the N_2 + H_2 plasma is intensively generated and confined into the hollow. This hollow cathode setup influences the activation process in the plasmas. The measured intensity of N_2^+ is employed as a parameter to describe this effect of processing parameters on the activation.

Figure 3 depicts the variation in N_2^+ peak intensity with the increasing pressure in the plasma diagnosis, with and without the use of the hollow cathode device. As predicted from [14,15], the ionization reaction presented in Equations (1)–(3) reduces with the increasing pressure of the N_2 + H_2 gas mixture. The yield of N_2^+ decreases monotonously with the increasing pressure. In the high-pressure range, the reaction cross-section for collision between the neutral nitrogen molecules and electrons reduces and results in less ionization. In addition, the mean free path becomes small enough to restrict

electron movement. When using the hollow cathode setup, this monotonous decrease in the yield of N_2^+ retards by itself. As had been discussed in [16,17], this is because the generated electrons by Equations (1)–(3) are confined in the hollow.

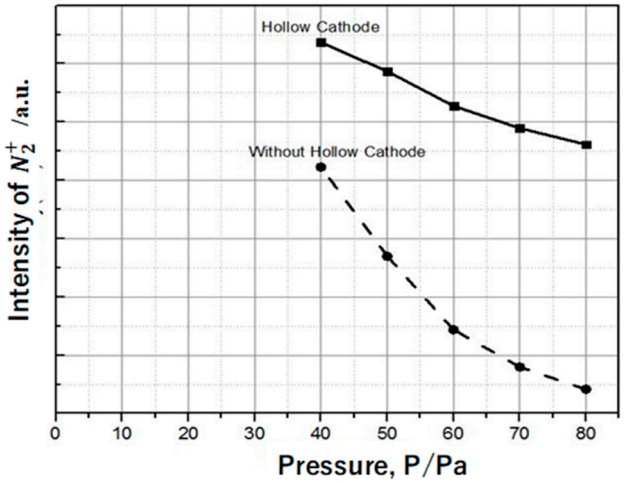

Figure 3. Variation in N_2^+ peak intensity with the increase in pressure in the plasma diagnosis, with and without the use of the hollow cathode device in case where V_{RF} = 250 V and V_{DC} = −500 V.

DC bias voltage was varied from −300 V to −600 V to investigate the enhancement of ionization with increasing the DC-bias. As depicted in Figure 4, the ionization process is enhanced by increasing V_{DC}. The RF-voltage was also varied from +100 V to +250 V to describe the enhancement of ionization with increasing the RF-voltage. As shown in Figure 5, the N_2^+ peak intensity linearly increases with the applied RF-voltage with and without the hollow cathode. This is because the ionization reaction cross-section in Equations (1)–(3) is proportional to the RF-voltage. Hence, higher DC-bias and RF-voltage is a necessary condition in this RF-DC plasma, nitriding at a low holding temperature.

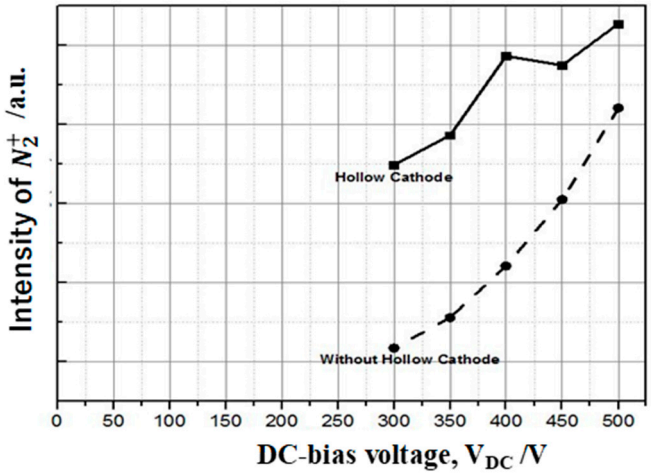

Figure 4. Variation in N_2^+ peak intensity with the increase in DC-bias voltage in the plasma diagnosis, with and without the use of the hollow cathode device in cases where p = 50 Pa and V_{RF} = 250 V.

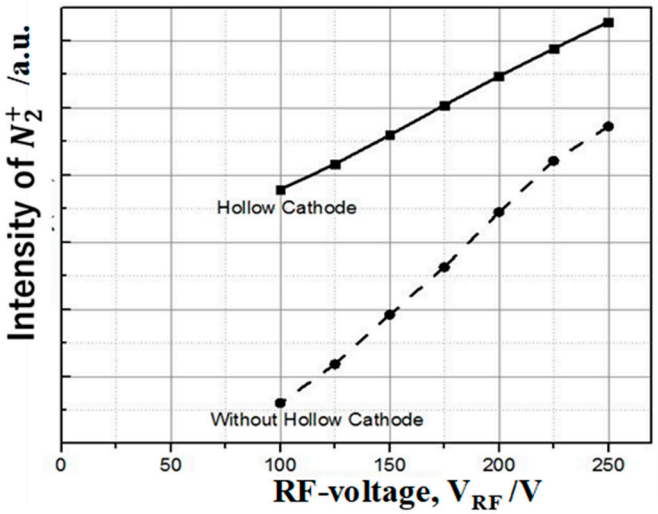

Figure 5. Variation in N_2^+ peak intensity with the increase in RF-voltage in the plasma diagnosis, with and without the use of the hollow cathode device in cases where p = 50 Pa and V_{DC} = −500 V.

3.3. Effect of Hydrgen Gas on the Detected Species

In addition to the nitrogen ionization from a mother species of N_2^+, the NH-radical plays an important role in plasma nitriding, as suggested in [15]. OES with wide and narrow scanning measurements was utilized to analyze the measured spectrum at the vicinity of Λ = 335 nm.

The measured spectrum at Λ = 335 nm was deconvoluted to two peak profiles at Λ = 334 nm and Λ = 336 nm, respectively, as shown in Figure 6. After Table 1, the former corresponds to the activated nitrogen molecule, and the latter is identified as a NH-radical. A very tiny disagreement is noticed between the measured spectrum and the superposed profile of the two peaks; this detection of NH-radicals has sufficient reliability for usage in parametric study in the following.

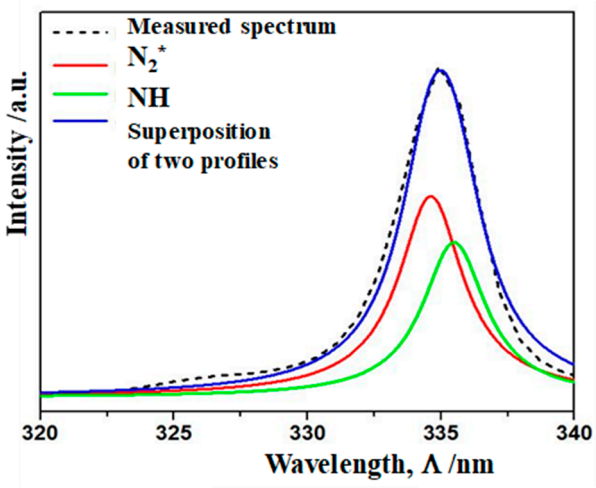

Figure 6. Detection of NH-radical by the N_2 + H_2 plasma diagnosis with the use of OES through wide and narrow scanning steps.

3.4. Effect of Hydrogen Gas Content on the NH Radicals

In the plasma nitriding with the use of N_2 + H_2 mixture gas, both N_2^+ ions and NH-radical work to supply the nitrogen atom flux onto the substrate surface for nitriding. Considering that only N_2^+ works as a mother ion to drive the nitrogen flux when using the N_2 gas, the effect of hydrogen gas content on nitriding is parametrically described by the ratio (R_{NH}) of the NH-radical peak intensity at Λ = 336.1 nm to the N_2^+-ion peak intensity at Λ = 394 nm in the plasma diagnosis experiment. As shown in Figure 7, this

ratio increases with the increase in hydrogen gas content and maximizes at $[H_2]$ = 20 to 25%. For $[H_2]$ > 25%, this ratio monotonously decreases with $[H_2]$. In the regime for 0 < $[H_2]$ < 25%, the N_2 + H_2 plasma is enriched with N_2^+-ion and NH-radicals enough to drive a sufficient nitrogen atom flux onto the substrate. On the other hand, it is poor in the population of NH-radical for $[H_2]$ > 25%. At the same time, the depletion of N_2 yields less N_2^+ ions since more H_2 molecules participate in the N_2-H_2 gas plasma mixture.

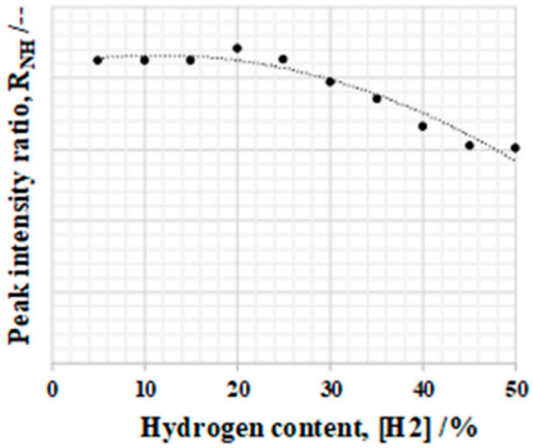

Figure 7. Variation in the peak intensity ratio for NH-radicals to N_2^+ ions with the increase in hydrogen gas content.

This poor population of NH-radicals in higher hydrogen gas content is explained by the hydrogen quenching effect [19]. In the presence of hydrogen molecules with high content, two activated nitrogen molecules of $N_2\left(A^3\sum_u^+\right)$ and $N_2\left(a'\sum_u^-\right)$ react to a more stable state of $N_2\left(X^1\sum_g^+\right)$ by the following reactions:

$$N_2\left(A^3\sum_u^+\right) + H_2 \rightarrow N_2\left(X^1\sum_g^+\right) + H + H \quad (4)$$

$$N_2\left(a'\sum_u^-\right) + H_2 \rightarrow N_2\left(X^1\sum_g^+\right) + H + H \quad (5)$$

Since two hydrogen atoms recombine to H_2, these reactions advance by themselves to quench the activation of nitrogen molecules and to reduce a yield of nitrogen atoms.

In the regime with less hydrogen molecule content, the above reactions become inferior to the following reaction between the enriched N_2^+ and H_2 and between H_2^+ and N_2;

$$N_2^+ + H_2 \rightarrow N_2H^+ + H \quad (6)$$

$$H_2^+ + N_2 \rightarrow N_2H^+ + H \quad (7)$$

This transient ion of N_2H^+ further reacts by its collision with electrons in the following,

$$N_2H^+ + e \rightarrow NH + H\ N_2H^+ + e \rightarrow N_2 + H \quad (8)$$

As suggested by [20,21], the reaction cross-section for N + N → N_2 is thought to be less than that for N + H → NH. These hydrogen atoms have the potential to react with nitrogen atoms from activated nitrogen molecules to yield NH-radicals.

3.5. Low Temperature Plasma Nitriding of AISI304 Stainless Steels

Two plasma nitriding experiments were performed to investigate the hydrogen gas content effect on the nitriding process with the use of the hollow cathode. AISI304 stainless steel disc specimen with a diameter of 20 mm and a thickness of 5 mm was employed as a work. In the first experiment, the hydrogen gas content was only varied to be 10%, 25% and

50%. The other plasma parameter was fixed in the pressure of 35 Pa, the DC of −600 V, and the RF-voltage of +250 V. AISI304 specimen was nitrided at 673 K for 14.4 ks. The surface hardness was measured by micro-Vickers testing with an applied load of 1 N (or 100 gf). Table 2 lists the measured surface hardness at each condition. The highest surface hardness is attained when $[H_2]$ = 25%. This proves that plasma diagnosis on the $N_2 + H_2$ plasmas is effective in determining the optimum nitriding conditions, and to make full use of NH radicals, as well as nitrogen ions.

Table 2. The hydrogen gas content effect on the surface hardness of nitrided AISI304 disc specimen at 673 K for 14.4 ks.

H_2 Percentage (%)	Hardness (HV)
No treatment	370
10	760
25	1100
50	680

In the second experiment, AISI304 specimen was nitrided at 623 K under the RF-voltage of +250 V, the DC-bias of −500 V, the pressure of 70 Pa and the gas flow rate ratio of 30 mL/min for hydrogen gas to 160 mL/min for nitrogen gas. Very few studies have reported DC-nitriding (or ion-nitriding) and the pulsed-DC-nitriding (or radical-nitriding) at 623 K; the nitrided layer thickness was limited to be negligibly thin [22,23]. Since the nitrogen diffusion governed those inner nitriding processes, a higher holding temperature was necessary to drive the nitriding process into the depth of the substrate. This plasma nitriding at 623 K provides a chance to reconsider the inner nitriding mechanism under the high nitrogen atom flux through the optimization of plasma conditions.

Figure 8 depicts the SEM image on the cross-section of the nitrided AISI304 substrate and its nitrogen mapping. The nitrided layer advanced to a depth of 50 μm, even at 623 K for 14.4 ks. Large grains were seen below the nitriding front end, while no grain boundaries were detected above this front. This suggests that the nitrided layer at 623 K has too fine grains distinguished by SEM with low magnification. This grain refinement process is discussed in later.

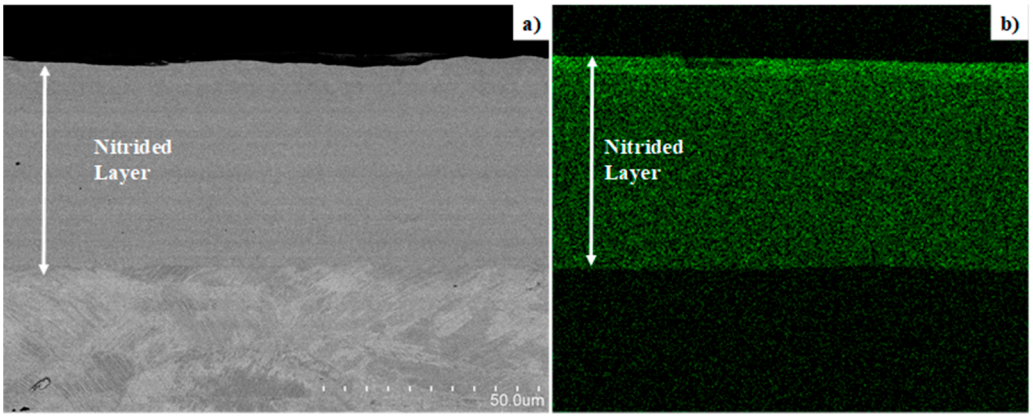

Figure 8. SEM image on the cross-section of nitrided AISI304 substrate at 623 K for 14.4 ks and its nitrogen mapping. (**a**) SEM image on the cross-section, and (**b**) nitrogen solute mapping.

After [4,8,24], this nitrided layer thickness is slightly proportional to the holding temperature (T_H) for 623 K < T_H < 693 K, while very few thicknesses were noticed in the normal nitriding at this low temperature [22,23]. In addition, this low temperature nitriding process is characterized by high nitrogen content, as depicted in Figure 8b. No iron and chromium nitrides precipitate in the nitrided layer so that nitrogen atoms are present as an interstitial solute in the iron lattice with high concentration. After pointwise detection by EDX in depth (d), the nitrogen content [N] at the surface reaches to [N] = 7.4 mass %

or 23.3 at %, while [N] = 4.5 mass % on average for 5 μm < d < 45 μm. Since the nitrogen solutes supersaturate the iron cells in the nitrided AISI304 stainless steels, the hardness is much higher than the original hardness of raw AISI304 (400 HV), due to the solid solution hardening mechanism. In fact, the surface hardness reaches 1640 HV; the average hardness is 1500 HV in the nitrided layer. These nitrogen and hardness depth profiles suggest that the high nitrogen atom flux at the surface drives nitrogen supersaturation, together with the nitrogen diffusion process, even at 623 K.

Let us describe this nitrogen supersaturation and diffusion co-process by EBSD analysis on the cross-section of a nitrided AISI304 substrate at 623 K for 14.4 ks. Figure 9a depicts the IPF mapping of depth. As seen in this map of the fur depth with d > 70 μm, the original AISI304 grains with a size of 40 to 50 μm, are divided into several colored and color-grated zones. In particular, each original AISI304 grain is changed to stripe-colored zones in 30 < d < 70 μm. On the other hand, the original granular microstructure in d < 30 μm is completely changed to have a very fine grain structure, with a size less than 0.1 μm or the resolution limit of EBSD after nitriding at 623 K.

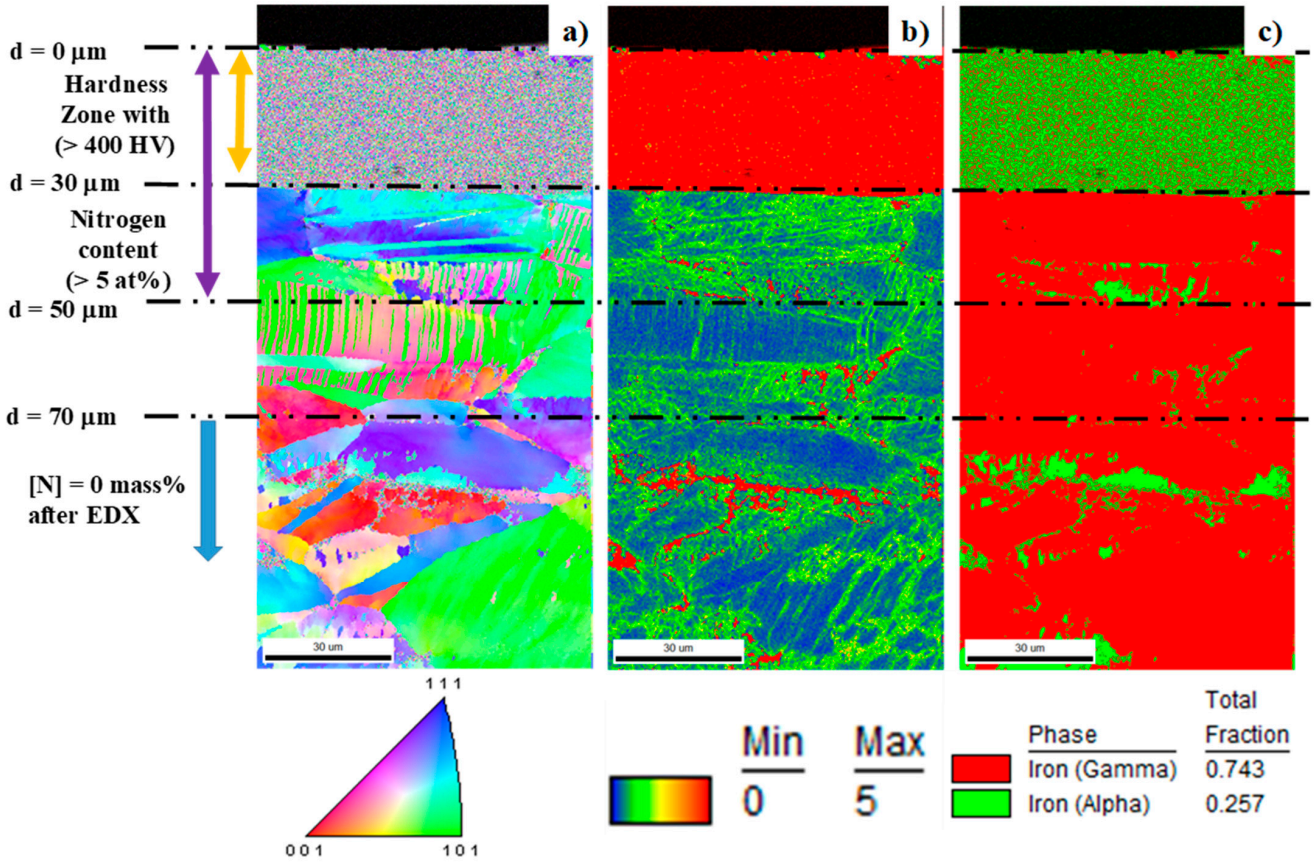

Figure 9. EBSD analysis on the microstructure at the cross-section of the nitrided AISI304 stainless steel substrate at 623 K for 14.4 ks after polishing and cleansing. (**a**) IPF profile, (**b**) KAM distribution, and (**c**) phase mapping.

Figure 9b,c show KAM distribution and phase mapping, respectively. The refined zone in d < 30 μm in Figure 9a has the highest misorientation angle and a fine two-phase structure. This KAM in Figure 9b denotes the plastic strain distribution. The transformation from γ-phase to α-phase in Figure 9c is induced by plastic straining under the nitrogen supersaturated state. Hence, the grain size of the original AISI304 is refined by high plastic straining everywhere in d < 30 μm, so that a huge amount of grain boundaries is generated together with the γ/α- and α/γ-zone boundaries. This refined layer is just equal to the high hardness layer with a high nitrogen content.

As stated in [4,25–27], the plastic strain in the above is induced by the strain incompatibility between the expanded lattices by nitrogen supersaturation and the original lattices without nitrogen interstitials. Those strain-incompatible zone boundaries form new fine grain and zone boundaries in the layer with d < 30 μm. Those new boundaries work as a network of nitrogen solute diffusion paths. The high intensity nitrogen atom flux at the surface penetrates through this network into the depth of substrate, together with nitrogen supersaturation.

In the conventional inner nitriding, the high hardness layer was simply coincidental to the high nitrogen content layer. In this nitriding at 623 K, driven by a high intensity nitrogen atom flux at the surface, the nitrogen supersaturation takes place homogeneously with nitrogen diffusion through the network and forms a grain-refined layer with high hardness. Once this nitrogen supersaturation localizes at d > 30 μm in Figure 9, the nitrogen diffuses to the depth only through the limited network. Due to this localized nitrogen diffusion, the homogeneous nitriding process terminates intermediately and induces the abrupt change in IPF, KAM and phase maps at d = 30 μm. Hardness gradually decreases in d > 30 μm, since the nitrogen supersaturation advances even by this localized nitrogen diffusion. This reflects the partial microstructure changes in the IPF profile, the locally high plastic strains in Figure 9b, and the localized phase transformation in Figure 9c.

As discussed in [26,27], this intermediate change from a homogeneous to heterogeneous nitriding process is eliminated by using fine-grained stainless-steel substrates. This suggests that the low temperature plasma nitriding by high nitrogen atom flux at the surface is essentially characterized by homogeneous inner nitriding, where the nitrogen supersaturation co-works with the nitrogen diffusion to drive the microstructure refinement, the plastic straining and phase transformation.

4. Conclusions

Plasma diagnosis with the use of OES is utilized to describe the effect of RF-DC plasma processing parameters and hydrogen gas content on the yield of N_2^+ ions and NH radicals. In particular, the yield ratio of NH-radicals to N_2^+ ions is employed as a parameter to investigate the effect of hydrogen gas content on the nitriding process. This ratio maximizes at a hydrogen content of 20 to 25%. When the hydrogen content is less than 20%, the reaction cross-section to yield the NH-radical increases with the hydrogen content, while this reaction cross-section significantly decreases with the increase in hydrogen content by the quenching effect. In particular, the yield of NH-radicals and N-ions significantly reduces with the increase in hydrogen content of up to 50% and results in low hardness. This optimization of hydrogen content in the nitriding process is demonstrated by the actual nitriding of AISI304 stainless steels at 673 K for 14.4 ks. The highest surface hardness is attained at this optimum hydrogen content. This proves that a sufficient amount of nitrogen atom flux at the substrate surface drives the inner nitriding process. This enriched nitrogen atom flux from the substrate surface drives the nitrogen supersaturation and diffusion co-process. Even at 623 K, when conventional nitriding only forms a very thin nitrided layer due to slow nitrogen diffusion, the AISI304 substrate can be nitrided to produce a thick nitrogen supersaturated layer with high hardness by the present plasma processing. The nitrogen supersaturation and diffusion co-process terminates by itself when the nitrogen diffusion network in the granular microstructure of AISI304 becomes too sparse to sustain the co-process.

In conventional plasma nitriding industries, the holding temperature is a main processing parameter since the inner nitriding process strongly depends on the nitrogen body-diffusion. In the presence of a rich nitrogen atom flux from the substrate surface to the depth, the inner nitriding takes place even at a much lower holding temperature. Since the nitrogen supersaturation and diffusion co-process is sustained by self-formation of the nitrogen diffusion network, the holding temperature can be lowered to broaden the application of plasma nitriding. In particular, the stainless-steel wires and tools for medical applications requires their hardening and strengthening without any additional alloying

metallic elements. The present low temperature plasma nitriding provides a solution by high hardening and strengthening them only with the enrichment of nitrogen solute contents in their depth.

Author Contributions: Conceptualization, T.A.; methodology, T.A.; validation, T.A., I.R.; formal analysis, E.E.Y.; investigation, T.A., I.R. and E.E.Y.; resources, T.A.; data curation, I.R.; writing—original draft preparation, T.A.; writing—review and editing, T.A.; visualization, I.R.; supervision, T.A. All authors have read and agreed to the published version of the manuscript.

Funding: This research received no external funding.

Institutional Review Board Statement: Not applicable.

Informed Consent Statement: Not applicable.

Acknowledgments: The authors would like to express their gratitude to D. Djoko and S.P. Sakti (University of Brawijaya, Indonesia) and A. Farghali (Graduate School of Engineering, University of Tokyo) for the help in experiments and discussion.

Conflicts of Interest: The authors declare no conflict of interest.

References

1. Bell, T. Surface engineering of austenitic stainless steel. *Surf. Eng.* **2002**, *18*, 415–422. [CrossRef]
2. Dong, H. S-phase surface engineering of Fe-Cr, Co-Cr and Ni-Cr alloys. *Int. Mater. Rev.* **2011**, *55*, 65–98. [CrossRef]
3. Lo, K.H.; Shek, C.H.; Lai, J.K.L. Recent developments in stainless steels. *Mater. Sci. Eng.* **2009**, *65*, 39–104. [CrossRef]
4. Aizawa, T. Low temperature plasma nitriding of austenitic stainless steels. Chapter 3. In *Stainless Steels*; IntechOpen: London, UK, 2018; Volume 3, pp. 31–50.
5. Djoko, D.J.; Aizawa, T. Formation of expanded martensite in plasma nitrided AISI420 stainless steel. In Proceedings of the 8th SEATUC Conference, Johor-Balu, Malaysia, 4 March 2014.
6. Farghali, A.; Aizawa, T. Nitrogen supersaturation process in the AISI420 martensitic stainless steels by low temperature plasma nitriding. *ISIJ Int.* **2018**, *58*, 401–407. [CrossRef]
7. Lu, S.; Zhao, X.; Wang, S.; Li, J.; Wei, W.; Hu, J. Performance enhancement by plasma nitriding at low gas pressure for 304 austenitic stainless steel. *Vacuum* **2017**, *145*, 334–339. [CrossRef]
8. Aizawa, T.; Shiratori, T.; Komatsu, T. Micro-/nano-structuring in stainless steels by metal forming and materials processing. Chapter 5. In *Electron Crystallography*; IntechOpen: London, UK, 2020; pp. 101–122.
9. Borgioli, F.; Galvanetto, E.; Bacco, T. Low temperature nitriding of AISI300 and 200 series austenitic stainless steels. *Vacuum* **2016**, *12*, 51–60. [CrossRef]
10. Farghali, A.; Aizawa, T.; Yoshino, T. Microstructure/mechanical characterization of plasma nitrided fine-grain austenitic stainless steels in low temperature. *J. Nitrogen* **2021**, *2*, 244–258. [CrossRef]
11. Tatarova, E.; Dias, F.M.; Gordiets, B.; Ferreira, C.M. Molecular Dissociation in N_2-H_2 Microwave Discharges. *Plasma Sources Sci. Technol.* **2005**, *14*, 19–31. [CrossRef]
12. Rosadi, I.; Djoko, D.; Sakti, S.P.; Yunata, E.E.; Aizawa, T. Plasma diagnosis on the mixture gas plasma state for nitriding process. In Proceedings of the 12th SEATUC Symposium, Yogyakarta, Indonesia, 3 March 2018; pp. 131–136.
13. Kim, Y.M.; Kim, J.U.; Han, J.G. Investigation on the Pulsed DC Plasma Nitriding with Optical Emission Spectroscopy. *Surf. Coat. Technol.* **2002**, *151*, 227–232. [CrossRef]
14. Sharma, M.K.; Saikia, B.K.; Bujarbarua, S. Optical Emission Spectroscopy of DC Pulsed Plasmas Used for Steel Nitriding. *Surf. Coat. Technol.* **2008**, *203*, 229–233. [CrossRef]
15. Tamaki, M.; Yoichi, T.; Yamamoto, N. The role of hydrogen in plasma nitriding: Hydrogen behavior in the titanium nitride layer. *Plasmas Ions* **2000**, *3*, 33–39. [CrossRef]
16. Katoh, T.; Aizawa, T.; Yamaguchi, T. Plasma assisted nitriding for micro-texturing onto martensitic stainless steels. In Proceedings of the 7th AWMFT 2014, Taipei, Taiwan, 9–12 November 2014.
17. Yunata, E.E. Characterization and Application of Hollow Cathode Oxygen Plasma. Ph.D. Thesis, Shibaura Institute of Technology, Tokyo, Japan, 2016.
18. Czerwiec, T.; Renevier, N.; Michel, H. Low-temperature plasma-assisted nitriding. *Surf. Coat. Technol.* **2000**, *131*, 267–277. [CrossRef]
19. Li, T.; Zhe, S. The quenching effect of hydrogen on the nitrogen in metastable state in atmospheric-pressure N_2-H_2 microwave plasma Torch. *Phys. Plasmas* **2014**, *21*, 67–72. [CrossRef]
20. Ricard, A.; Oseguera-Pena, J.E.; Falk, L.; Michel, H.; Gantois, M. Active species in microwave post-discharge for steel-surface nitriding. *IEEE Trans. Plasma Sci.* **1990**, *18*, 940–944. [CrossRef]
21. Guo, J.-Y.; Kuo, Y.-K.; Wang, H.-P. A facile nitriding approach for improved impact wear of martensitic cold-work steel using H_2/N_2 mixture gas in an AC pulsed atmospheric plasma jet. *Coatings* **2021**, *11*, 1119. [CrossRef]

22. Saito, K. Introduction to Ion Nitriding in Hokunetsu. 2018. Available online: http://hokunetsu.com/products/003/ (accessed on 14 February 2022).
23. Taktak, S.; Güneş, I.; Ulker, S. Effect of pulse plasma nitriding on tribological properties of AISI 52100 and 440C steels. *Int. J. Surf. Sci. Eng.* **2014**, *8*, 39–56. [CrossRef]
24. Aizawa, T.; Shiratori, T.; Komatsu, T. Integrated manufacturing of fine-grained stainless steels for industry and medicals. Chapter 1. In *Engineering Steels and High Entropy-Alloys*; IntechOpen: London, UK, 2020; pp. 1–26.
25. Aizawa, T.; Yoshino, T. Plastic straining for microstructure refinement in stainless steels by low temperature plasma nitriding. In Proceedings of the 12th SEATUC Conference Yag-Yakarta, Jakarta, Indonesia, 12 March 2018; pp. 11–16.
26. Aizawa, T.; Yoshino, T.; Shiratori, T.; Yoshihara, S.-I. Grain size effect on the nitrogen supersaturation process into AISI316 at 623 K. *ISIJ Int.* **2019**, *59*, 1886–1892. [CrossRef]
27. Aizawa, T.; Yoshihara, A.-I. Inner nitriding behavior and mechanism in stainless steels at 753 K and 623 K. *SEATUC J. Sci. Eng.* **2019**, *1*, 13–20.